

## Structure and stability of $2H_a$ -MoS<sub>2</sub> at high pressure and low temperatures

Alexander F. Goncharov<sup>1</sup>, Maxim Bykov<sup>1,2</sup>, Elena Bykova<sup>1</sup>, Konstantin Glazyrin<sup>3</sup>, Vitali Prakapenka<sup>4</sup>,  
Zi-Yu Cao<sup>5</sup> and Xiao-Jia Chen<sup>5</sup>

<sup>1</sup>*Earth and Planets Laboratory, Carnegie Institution of Washington, Washington, DC 20015, USA*

<sup>2</sup>*Department of Mathematics, Howard University, Washington, DC 20059, USA*

<sup>3</sup>*Photon Science, DESY, Notkestrasse 85, DE-22607 Hamburg, Germany.*

<sup>4</sup>*Center for Advanced Radiation Sources, University of Chicago, Chicago, Illinois 60637, USA*

<sup>5</sup>*Center for High Pressure Science and Technology Advanced Research, Shanghai 201203, China*

HPSTAR  
1034-2020



(Received 16 June 2020; revised 20 July 2020; accepted 24 July 2020; published 17 August 2020)

X-ray synchrotron diffraction (XRD) measurements of single-crystal and powder molybdenum disulfide MoS<sub>2</sub> are performed at pressures ( $P$ ) up to 78 GPa and temperatures ( $T$ ) of 20 to 298 K in diamond-anvil cells. The results on single crystals demonstrate a sharp pressure induced isosymmetric phase transition of  $2H_c$  to  $2H_a$  modification at 23 GPa at 40 and 300 K. The structure of the high-pressure  $2H_a$  phase previously inferred theoretically and from powder XRD data is confirmed by our single-crystal XRD data solution, which also definitively determines the atomic positions as a function of pressure. No additional periodicity (commensurate or incommensurate) or distortion is found in the whole  $P$ - $T$  range of this study. These results suggest that a previously proposed hypothetical charge-density-wave phase does not host pressure induced superconductivity experimentally found above 90 GPa.

DOI: [10.1103/PhysRevB.102.064105](https://doi.org/10.1103/PhysRevB.102.064105)

MoS<sub>2</sub> is an archetypal quasi-two-dimensional (2D) transition-metal dichalcogenide (TMD) material, which holds promise for technological applications as an alternative to graphene albeit with a nonzero band gap. Moreover, a heavily gated MoS<sub>2</sub> demonstrates superconducting behavior [1,2]. Tuning the doping level in TMD reveals a number of electronic states and orders including charge-density-wave (CDW) and superconductivity (SC). A generic phase diagram of TMD as a function of the doping level typically includes metallization of a semiconducting phase following by the emergence of CDW and SC states, which are normally competing, e.g., Ref. [3]. The interplay between charge/magnetic long-range ordered states and SC is one of the most debated topics in modern condensed-matter physics, solving which could potentially result in a breakthrough in understanding of high-temperature SC.

Application of pressure is an alternate way to tune the electronic properties of TMD, which is somewhat similar to doping. At ambient conditions MoS<sub>2</sub> crystallizes in a hexagonal layered structure with two S-Mo-S layers in the unit cell; the atoms form the AbA-BaB sequence along the  $c$  axis, which corresponds to a  $2H_c$  polytype [4]. This phase is an indirect band-gap semiconductor [5], which becomes a direct-gap semiconductor in a monolayer state (like graphene) [6] opening possibilities for band-gap engineering. Meanwhile, the bulk  $2H_c$  MoS<sub>2</sub> is expected to transform to a semimetallic state via the indirect band-gap closure at 25–29 GPa [5,7,8], while the complete direct band-gap closure is expected at higher compressions [8]. The electrical conductivity measurements at high pressures indeed show a dramatic increase at 10–19 GPa suggesting the approaching band-gap closure

[9,10]. However, this electronic transition is complicated by an isosymmetric phase transition to another polytypic modification ( $2H_a$ ) at about 25 GPa, where the layers slide resulting in the AbA-CbC atomic sequence, so Mo atoms of different layers have the same ( $x,y$ ) positions [5]. This transformation has been detected using powder x-ray diffraction (XRD) and Raman and optical spectroscopy [including infrared (IR)] [10–12]; the experiments show a broad pressure range of the phase coexistence (16–40 GPa), which makes it difficult to associate the electronic and structural transitions definitively.

The metallic properties of  $2H_a$  MoS<sub>2</sub> have been definitively established above 35 GPa based on optical spectroscopy and temperature-dependent electrical conductivity measurements [9–11]. The low-temperature resistivity curves demonstrated irregularity in a form of hump at 130–190 K increasing with pressure below 24 GPa and constant at higher pressures [10,13,14]. Moreover, low-temperature Raman experiments show an additional mode at 174 cm<sup>-1</sup> [14], which was tentatively assigned to the Brillouin-zone boundary ( $K$  and  $M$  points) transverse-acoustic phonons [15]. These phenomena were discussed in connection to a possible CDW state in MoS<sub>2</sub> at these conditions, similar to that previously detected in other TMD (e.g.,  $2H_a$  NbSe<sub>2</sub>) [16–18], where doping or pressure first results in a CDW state being suppressed by a SC state on the later stage. Superconductivity has been reported in MoS<sub>2</sub> above 90 GPa [13]; the critical temperature ( $T_c$ ) increases with pressure, but it remains almost constant (12 K) above 120 GPa up to the maximum pressure of 220 GPa that has been reached. In this paper, we comprehensively examine the structure of MoS<sub>2</sub> of both  $2H_c$  and  $2H_a$  polytypes and the phase-transition line between them at 40–298 K

using synchrotron single-crystal XRD on carefully selected samples. We show that the transition pressure range reduces drastically in single crystals. We provide first definitive structural determination of  $2H_a$  MoS<sub>2</sub> and find no periodic lattice distortion (PLD) [19], which could be connected to CDW behavior in a broad  $P$ - $T$  range up to 78 GPa and from 20 to 298 K, demonstrating that previous observations [10,13,14] were not related to PLD. This result is assigned to a difference in the electronic properties of MoS<sub>2</sub> compared to TiSe<sub>2</sub>, NbSe<sub>2</sub>, and TaS<sub>2</sub>, where a different number of the valence electrons are involved for the formation of the electronic bands near the Fermi level.

The experiments were performed in diamond-anvil cells of symmetric and BX-90 type [20]. Ne and He pressure transmission media have been used to ensure the best hydrostatic conditions at low temperature. These gases were loaded in the diamond-anvil cells (DACs) at room temperature using a high-pressure gas loading systems at the Earth and Planets Laboratory and the extreme conditions beamline (ECB) at Petra III, DESY. Rhenium foil preindented to 30–40  $\mu\text{m}$  thickness served as a gasket. The diamond anvils had flat culets 200  $\mu\text{m}$  in diameter. The anvils of standard type were used for the powder XRD and the anvils with a conical support [21] for the single-crystal experiments, respectively. These DACs had an angular opening for x ray of  $\pm 22^\circ$  and  $\pm 34^\circ$ , respectively. For the powder experiments, the sample was thoroughly grinded before loading and the amount of material was kept small to avoid bridging between the anvils. For the single-crystal experiments, the two samples were chosen out of some 50 pieces tested by examining their quality in the identical conditions (screening using a single diamond anvil with a large culet). The single-crystal samples were of 20–40  $\mu\text{m}$  in linear dimensions and a few  $\mu\text{m}$  in thickness. Single-crystal synchrotron XRD experiments were performed in a He cryostat at ECB, Petra III, DESY by collecting patterns at different angle positions of a DAC while it rotates along the  $\omega$  rotation axis (vertical) with the samples carefully centered on a rotation center. The XRD patterns were acquired with a  $0.5^\circ$  interval with a collection time of 1–4 s. The x-ray wavelength was 0.291  $\text{\AA}$ . The instrumental model was calibrated using a single crystal of orthoenstatite [(Mg<sub>1.93</sub>Fe<sub>0.06</sub>)(Si<sub>1.93</sub>, Al<sub>0.06</sub>)O<sub>6</sub>,  $Pbca$  space group,  $a = 8.8117(2)$ ,  $b = 5.18320(10)$ , and  $c = 18.2391(3)$   $\text{\AA}$ ]. Pressure in single-crystal experiments was measured *in situ* at low temperatures using a ruby ball sensor positioned in the high-pressure cavity; to calculate the wavelength shift of the ruby  $R_1$  line at various temperatures; we concomitantly measured the reference ambient pressure spectrum of the ruby ball positioned on the diamond-anvil table. We used the ruby pressure calibration, which takes into account a change in the temperature slope of the ruby line wavelength with pressure [22]. Low-temperature powder XRD experiments were performed using a cryocooler jet at the GSECARS beamline at the APS, ANL. In the powder XRD experiments, the pressure was determined using Au pressure gauge calibrated in  $P$  and  $T$  [23]. The x-ray wavelength was 0.3344  $\text{\AA}$ .

Three separate XRD synchrotron experiments were performed that differ by the experimental arrangement (single crystal vs powder), the light source (GSECARS at APS, ANL, and ECB at Petra III, DESY), experimental path (isotherms

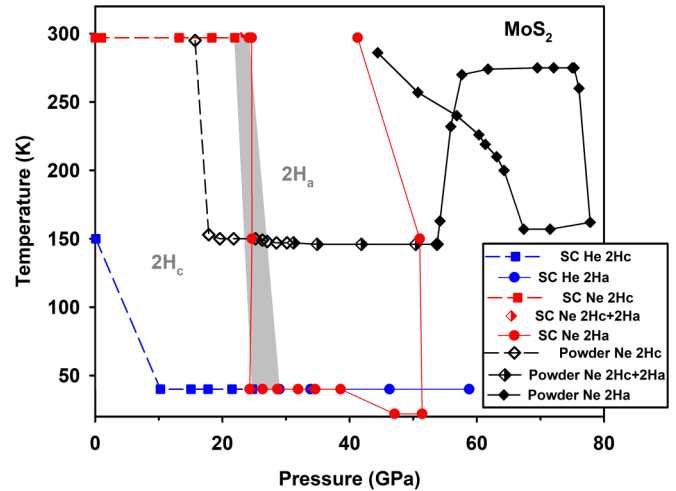


FIG. 1. Phase diagram of MoS<sub>2</sub> and experimental pressure-temperature ( $P$ - $T$ ) pathways of our experiments. The experimental conditions are labeled according to the type of the XRD experiment, transmission medium, and phase. The experimental sequences start at low  $P$  and high temperature and pass the transition isothermally at 40 K (down to 22 K), 150 K, and 300 K. The gray dashed area corresponds to the phase coexistence range determined in our single-crystal XRD experiments.

at 40–298 K), and the pressure medium (He and Ne). The experimental pathways are shown in Fig. 1. In the powder-diffraction experiment, we increased pressure at 150 K. The  $2H_c$  to  $2H_a$  transition has been observed similar to the previous reports at room temperature [10,13]. However, the  $2H_a$  phase was first detected at 31 GPa, where a shoulder appeared at the (002) Bragg peak, which is much higher than in a similar experiment at room temperature (23 GPa) (e.g., Ref. [10]). The pressure range of the transition, where both phases are detected, is very broad, extending up to 50 GPa, which is again higher than that at 300 K. These observations suggest that an increased deviatoric stress field at low temperatures has a substantial effect on the transition by broadening and shifting it to higher pressures. In contrast, single-crystal experiments showed very sharp transitions, narrower than 4 GPa, determined by either the phase coexistence range or by the pressure step over which we observed the complete phase change. The phase line determined in single-crystal XRD measurements has a negative pressure slope (Fig. 1), which is consistent with the powder XRD data of this work and Raman measurements of Refs. [10,14]. The variation in the observed behavior between powder and single-crystal samples cannot be correlated with different pressure media, but is likely due to deviatoric stresses in the DACs (likely uniaxial), affecting differently the transition in randomly oriented crystallites in powder and oriented single crystals. The experiments reached the maximum pressures between 52 and 78 GPa, and only the  $2H_a$  phase was observed above the  $2H_c$ - $2H_a$  transition as stipulated below.

Our single-crystal diffraction data (see Figs. 2–4 and Table S1 of the Supplemental Material [24]) allowed the structural solutions in both the high- and the low-pressure phases. Bragg peak intensities were extracted by means of Rigaku CRYSTAL-SPRO software [25] and analyzed by means of Olex2 [26]

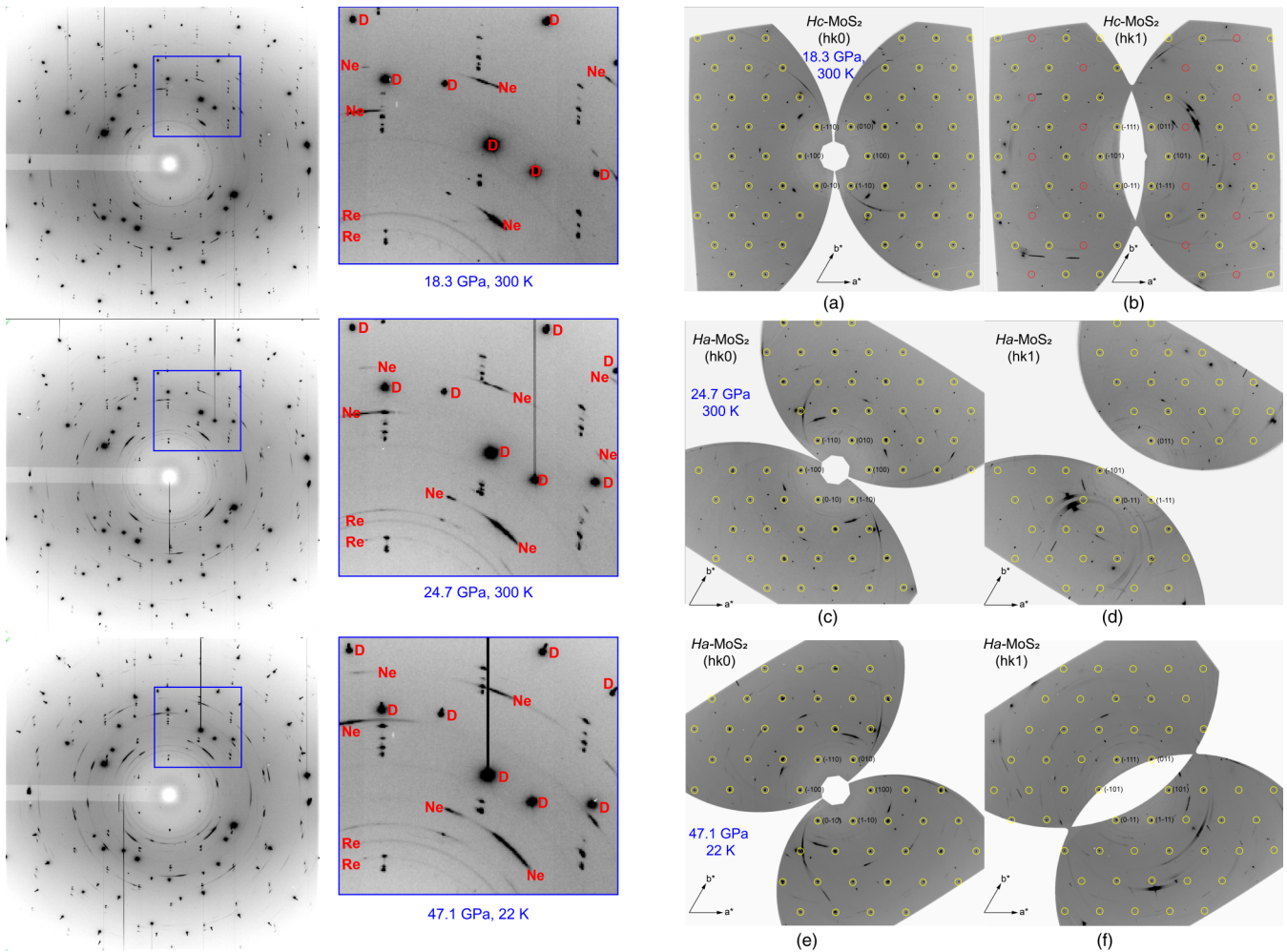


FIG. 2. Single-crystal XRD data. Left panel: Wide angle scans at various pressures corresponding to  $2H_c$  (18.3 GPa, 300 K) and  $2H_a$  (at 24.7 GPa, 300 K, and 47.1 GPa, 40 K) phases; insets show zoomed in parts of the diffractograms, which detail the assignment of the observed XRD features. Right panel: Reconstructed  $(hk0)$  and  $(hk1)$  precession images of MoS<sub>2</sub> at selected pressures. In each projection, the indexed reflections are shown as encircled reflection spots. No superlattice reflections are observed at any of the pressure-temperature points. (a),(b) Low-pressure  $2H_c$ -MoS<sub>2</sub> phase. Note that in the  $2H_c$ -MoS<sub>2</sub> structure Mo and S atoms occupy Wyckoff sites  $2c$  and  $4f$  respectively, leading to the weakening of reflections  $hkl$  with  $l = 2n + 1$  and  $h-k = 3n$ . Such reflections are marked by red circles. (c)-(f) High-pressure  $2H_a$ -MoS<sub>2</sub> phase. Note that in this phase Mo occupies Wyckoff site  $2a$ , which implies that the intensities of reflections  $hkl$  with  $l = 2n + 1$  are defined only by the scattering of S atoms. This leads to a significant weakening of all reflections with  $l = 2n + 1$ . The x-ray wavelength was 0.291 Å.

(with SHELX [27] backend) and additionally with Jana2006 [28]. The structural refinements at close to ambient conditions agree well with the  $2H_c$  phase structural parameters reported previously [29]. Upon the exertion of pressure, the  $H_c$  phase preserves to approximately 22 GPa. The refined value of the S fractional coordinate  $z_S$  changes with pressure significantly representing substantially stronger interlayer vs intralayer contraction (Fig. 4) (cf. Ref. [13]). Indeed, between 0 and 22 GPa, the shortest Mo-S intralayer distance changes by only 2.2% (from 2.403 to 2.349 Å) while the shortest S-S intermolecular distance changes by 16.6% (from 3.503 to 2.92 Å). Our single-crystal XRD measurements detect a very abrupt  $2H_c$  to  $2H_a$  transition, where only in one occasion we were able to observe the phase coexistence at 23 GPa at 300 K (Figs. 1 and 3). At the  $2H_c$  to  $2H_a$  isosymmetric transition, the site symmetry (Wyckoff position) of the Mo atoms changes,

which results in redistributions in intensities of a number of Bragg reflections (Fig. 2). The pressure dependencies of the lattice parameters (Fig. 5) are very similar for both single-crystal data sets but they differ from the powder data (see below), however, all data seem to merge above 50 GPa, where the transition completes for the powder sample.

Powder XRD results reveal a good correspondence to the previously predicted and observed  $H_a$  MoS<sub>2</sub> (see Fig. S1 of the Supplemental Material [24]) in the Bragg peak positions and a change in the peak intensities compared to  $H_c$  MoS<sub>2</sub> [5,10,13]. However, because of the texture (a limited number of grains), the observed peak intensities showed a large discrepancy with the calculated ones, so the Rietveld refinement could not be performed. Thus, the positional parameters of S atoms ( $z_S$ ) could not be defined from the powder data. Chi *et al.* [13] performed the Rietveld refinement of their

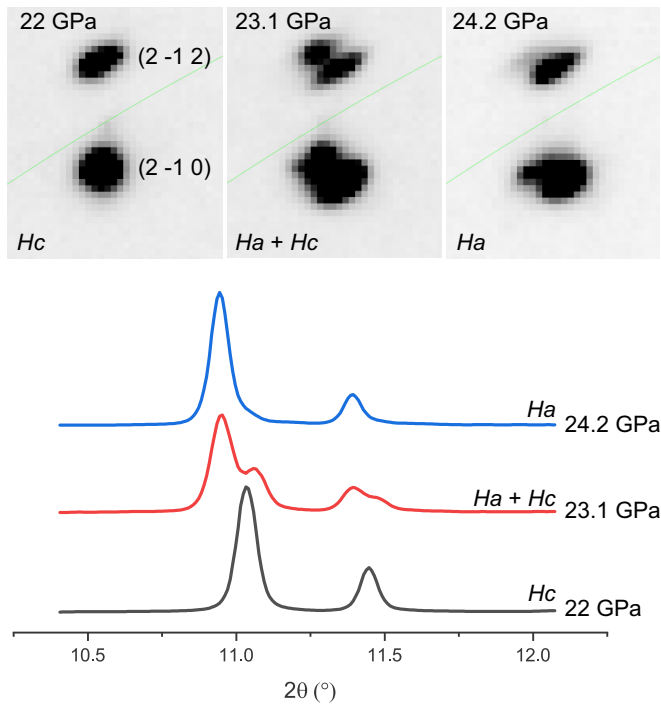


FIG. 3. Single-crystal XRD data across the phase transition. Top: Diffractograms of selected Bragg reflections through the  $H_c$  to  $H_a$  phase transition at 300 K in Ne medium. Bottom: the integrated 1D XRD patterns. The x-ray wavelength is 0.291 Å.

data and obtained a very weakly pressure-dependent structural parameter  $z_S = 0.614$  in  $H_c$  and  $z_S = 0.61$  in  $H_a$  polytypes (Fig. 4), which is inconsistent with our single-crystal results. The lattice parameters, which were refined from our powder XRD data, show a discontinuous change at the transition (Fig. 5). The results on the lattice parameters show a good correspondence with the data reported previously at 300 K

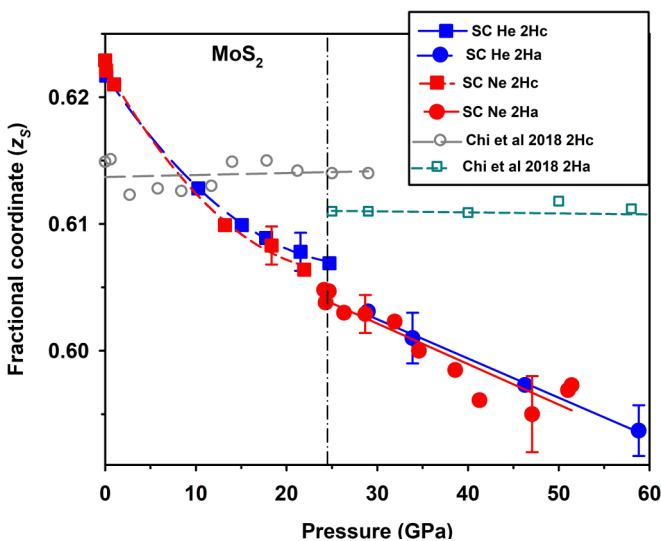


FIG. 4. The sulfur  $z$  structural coordinate parameter. Filled symbols: single-crystal XRD data. The results of the Rietveld refinement of the powder XRD data of Ref. [13] are shown for comparison. We refer to Fig. 1 for sample temperatures.

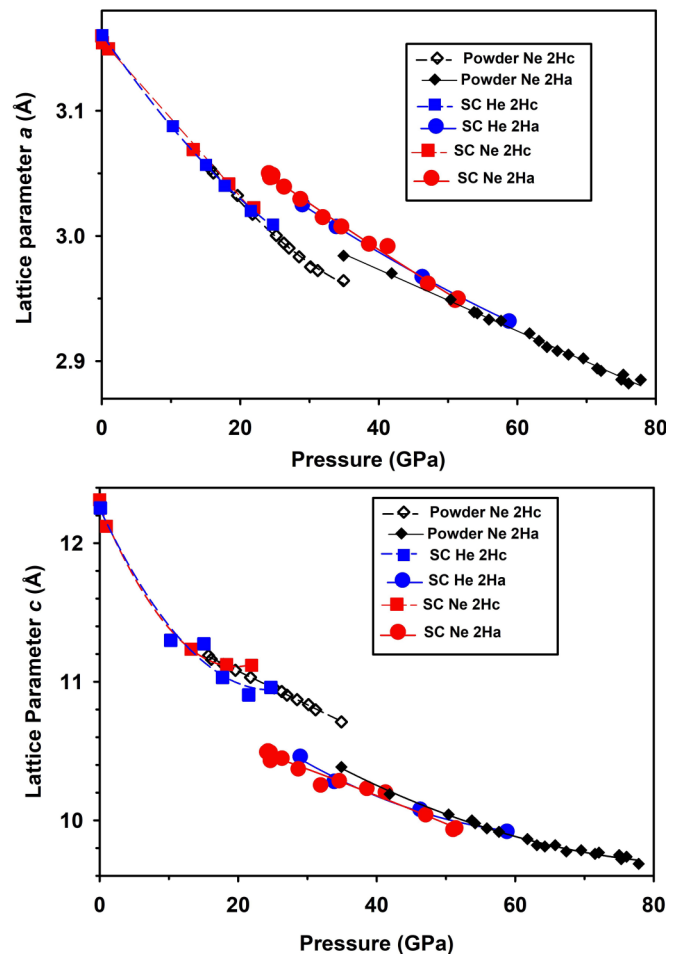


FIG. 5. The lattice parameters of  $\text{MoS}_2$  as a function of pressure. The symbols correspond to the data of this work determined by refining powder and single-crystal XRD data; they are labeled according to the type of experiments, pressure medium, and the phase. The error bars are within the size of the symbol. We refer to Fig. 1 for sample temperatures.

in the pressure ranges of stability of  $2H_c$  and  $2H_a$  phases but there are deviations in the pressure span of the transition (see above) and in the lattice parameters in the transition range (Fig. S2 [24]). Our single-crystal (Figs. 3 and 5) and powder XRD (Fig. S2 [24]) data consistently show that the lattice parameter  $a$  discontinuously increases at the transition, while the lattice parameter  $c$  drops. This is in agreement with the powder XRD results of Ref. [10] and theoretical calculations [5] but at odds with recent powder XRD data [13]. This discrepancy cannot be due to the difference in the stress field or temperature because our experiments show a similar behavior of the lattice parameters for the transitions recorded at various temperatures, in different transmission media, and using both single-crystal and powder-diffraction techniques. Please also note that the volumes of Ref. [13] show a large discontinuity at the transition, while our data show a much smaller volume change (Fig. S3 [24]). However, this discrepancy in the lattice parameters and volumes (Figs. S2 and S3 [24]) is only in the transition pressure range. In this regard, our single-crystal XRD data (Figs. 3 and 5) are certainly superior in accuracy,

while we believe that the powder data of Ref. [13] did not capture well the transition pressure range.

Both powder and single-crystal sets of data (Figs. 2–5, S2, and S3 [24]) definitively show that the  $2H_a$  phase remains stable in the  $P$ - $T$  range explored here (Fig. 1) at pressures above the  $2H_c$ - $2H_a$  transition. We do not observe any new Bragg reflection, nor do we detect any additional anomalies in the unit-cell parameters (Fig. 5) at low temperatures down to 22 K and up to the highest pressures that we reached (up to 78 GPa). This is mostly clear from the observations of the reciprocal space (Fig. 2), where any additional periodicity signaling PLD would be seen as extra reflection spots positioned along the lines connecting the reciprocal points of the original lattice, which are apparently missing (e.g., SnS<sub>2</sub> in Ref. [30]). Concerning different temperature conditions, the lattice parameters and the unit-cell volume (Figs. 5, S2, and S3 [24]) are basically indistinguishable and show no CDW related detectable anomaly in the whole pressure range of observation. The  $P$ - $T$  conditions explored here favorably overlap with those where electrical conductivity and Raman spectroscopy detected the anomalies [10,13,14], which were tentatively connected with a possible CDW ordering, making clear that these are not related to CDW ordering, at least to the one that would be connected to PLD. Thus, we conclude that there is no strong periodic lattice distortion that develops in  $2H_a$  MoS<sub>2</sub> up to at least 60 GPa at 40 K (less definitively to 78 GPa at 150 K), suggesting that there is no conventional CDW state in this regime [31,32]. Even though our XRD data do not cover the whole pressure range adjacent to the superconducting state ( $>90$  GPa), they clearly rule out that the observation of Refs. [10,13,14] are related to PLD and likely the CDW state. Indeed, the emergence of CDW in metallic TMD is commonly explained as due to the wave-vector dependent electron-phonon coupling driving the lattice instability [33,34]—the effect which could not be missed in our single-crystal XRD results.

Overall, our data demonstrate the stability of  $2H_a$  MoS<sub>2</sub> in a very wide  $P$ - $T$  domain (Fig. 1) which is very likely adjacent to the superconducting state above 90 GPa [13]. In contrast to other metallic TMDs, such as TiSe<sub>2</sub>, NbSe<sub>2</sub>, and TaS<sub>2</sub>, there is no clearly identified CDW state, which would precede the superconducting state. In the past, the competition between CDW and superconductivity has been considered as a common prerequisite for emergence of superconductivity in TMD. However, MoS<sub>2</sub> appears to be a stand-alone case in that high-pressure superconductivity in the  $2H_a$  structural modification emerges using another mechanism. Rösner *et al.* [35] noticed this possibility in their first-principles calculations in a monolayer MoS<sub>2</sub> upon electronic doping and suggested that the difference is in the number of valence electrons in the metal, which is one or two more than in Nb, Te, and Ta. These latter TMDs indeed demonstrate the conventional CDW followed by SC upon doping or compression. Thus, different electronic bands are responsible for the electronic instabilities in MoS<sub>2</sub>, which might result in the inversion of the phase diagram in that the CDW state would appear at higher pressures than SC, which is much higher than investigated here.

The stability of  $2H_a$  MoS<sub>2</sub> in a wide  $P$ - $T$  domain is in agreement with first-principles theoretical calculations [5],

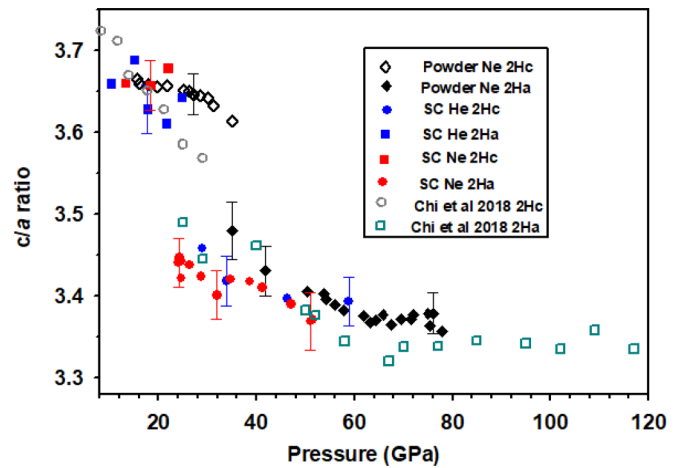


FIG. 6. The  $c/a$  lattice parameter ratio of MoS<sub>2</sub> as a function of pressure. The filled symbols correspond to the data of this work determined by refining powder and single-crystal XRD data; they are labeled according to the type of experiments, pressure medium, and the phase. We refer to Fig. 1 for sample temperatures. Open symbols are from the Ref. [13] determined from synchrotron powder XRD data.

which did not find any lattice instability including CDW. On the other hand, the same calculations also found that SC is improbable due to a small electron-phonon coupling. The experimentally found emergence of SC above 90 GPa is likely due to a combination of low dimensionality and a possible pressure-induced electronic Lifshitz transition [5,13,36]. The proximity of  $2H_a$  MoS<sub>2</sub> to the Lifshitz transition is indicated by a minimum in the  $c/a$  lattice parameter ratio (Fig. 6) (e.g., Ref. [37]). Yet an alternative scenario would be an appearance at low temperatures of another electronic order such as in an excitonic insulator [38,39] hosted by semiconductor and semimetallic states of MoS<sub>2</sub> close to the insulator-metal transition that occurs upon or close to the  $2H_c$  and  $2H_a$  transition. Such an excitonic insulator mechanism has been proposed to explain CDW and the periodic lattice distortion state in 1T-TiSe<sub>2</sub> [40]. However, the absence of PLD in MoS<sub>2</sub> points to a possibility of a pure electronic origin of putative CDW in this material, providing a natural explanation to anomalous electronic conductivity and low-temperature Raman peaks reported previously [10,13,14].

In conclusion, we present single-crystal XRD data in MoS<sub>2</sub> in a wide  $P$ - $T$  domain where previous study detected an isosymmetric phase transition between  $2H_c$  and  $2H_a$  polytypes and inferred a possible CDW behavior preceding a superconducting state at 95 GPa. Our experiments show that the transition pressure range reduces drastically in single crystals compared to powder suggesting a possible coupling with deviatoric stresses. Our single-crystal XRD yields definitive structural determination of the high-pressure  $2H_a$  MoS<sub>2</sub> phase and find no structural distortion or symmetry break, which could be connected to CDW behavior in a broad  $P$ - $T$  range up to 78 GPa and from 20 to 298 K. These results suggest that previous electrical conductivity and Raman anomalous behavior are not related to PLD, but instead could be due to a purely electronic transformation such as the Lifshitz transition

and the emergence of a long sought excitonic insulator state. The difference in behavior of MoS<sub>2</sub> compared to TiSe<sub>2</sub>, NbSe<sub>2</sub>, and TaS<sub>2</sub> demonstrating CDW states is likely because of a different number of the valence electrons that are involved for the formation of the electronic bands near the Fermi level.

Parts of this research were carried out at the Extreme Conditions Beamline (P02.2) at DESY, a member of Helmholtz Association (HGF). Parts of this work were performed at GeoSoilEnviroCARS (The University of Chicago, Sector 13), Advanced Photon Source (APS), Argonne National Labora-

tory. GeoSoilEnviroCARS is supported by the National Science Foundation - Earth Sciences (EAR - 1634415) and Department of Energy- GeoSciences (DE-FG02-94ER14466). The Advanced Photon Source is a U.S. Department of Energy (DOE) Office of Science User Facility operated for the DOE Office of Science by Argonne National Laboratory under Contract No. DE-AC02-06CH11357. M.B. and A.F.G. acknowledge support of the Army Research Office (Grants No. 56122-CH-H and No. 71650-CH W911NF-19-2-0172) and the Deep Carbon Observatory. E.B. and A.F.G. acknowledge support of the Carnegie Institution of Washington.

- 
- [1] J. T. Ye, Y. J. Zhang, R. Akashi, M. S. Bahramy, R. Arita, and Y. Iwasa, *Science* **338**, 1193 (2012).
- [2] K. Taniguchi, A. Matsumoto, H. Shimotani, and H. Takagi, *Appl. Phys. Lett.* **101**, 042603 (2012).
- [3] X.-M. Zhao, K. Zhang, Z.-Y. Cao, Z.-W. Zhao, V. V. Struzhkin, A. F. Goncharov, H.-K. Wang, A. G. Gavriliuk, H.-K. Mao, and X.-J. Chen, *Phys. Rev. B* **101**, 134506 (2020).
- [4] H. Katzke, P. Tolédano, and W. Depmeier, *Phys. Rev. B* **69**, 134111 (2004).
- [5] L. Hromadová, R. Martoňák, and E. Tosatti, *Phys. Rev. B* **87**, 144105 (2013).
- [6] K. F. Mak, C. Lee, J. Hone, J. Shan, and T. F. Heinz, *Phys. Rev. Lett.* **105**, 136805 (2010).
- [7] H. Guo, T. Yang, P. Tao, Y. Wang, and Z. Zhang, *J. Appl. Phys.* **113**, 013709 (2013).
- [8] C. Espejo, T. Rangel, A. H. Romero, X. Gonze, and G. M. Rignanese, *Phys. Rev. B* **87**, 245114 (2013).
- [9] A. P. Nayak, S. Bhattacharyya, J. Zhu, J. Liu, X. Wu, T. Pandey, C. Jin, A. K. Singh, D. Akinwande, and J.-F. Lin, *Nat. Commun.* **5**, 3731 (2014).
- [10] Z.-H. Chi, X.-M. Zhao, H. Zhang, A. F. Goncharov, S. S. Lobanov, T. Kagayama, M. Sakata, and X.-J. Chen, *Phys. Rev. Lett.* **113**, 036802 (2014).
- [11] P. Shen, Q. Li, H. Zhang, R. Liu, B. Liu, X. Yang, Q. Dong, T. Cui, and B. Liu, *Phys. Status Solidi B* **254**, 1600798 (2017).
- [12] R. Aksoy, Y. Ma, E. Selvi, M. C. Chyu, A. Ertas, and A. White, *J. Phys. Chem. Solids* **67**, 1914 (2006).
- [13] Z. Chi, X. Chen, F. Yen, F. Peng, Y. Zhou, J. Zhu, Y. Zhang, X. Liu, C. Lin, S. Chu, Y. Li, J. Zhao, T. Kagayama, Y. Ma, and Z. Yang, *Phys. Rev. Lett.* **120**, 037002 (2018).
- [14] Z.-Y. Cao, J.-W. Hu, A. F. Goncharov, and X.-J. Chen, *Phys. Rev. B* **97**, 214519 (2018).
- [15] A. Molina-Sánchez and L. Wirtz, *Phys. Rev. B* **84**, 155413 (2011).
- [16] M. Naito and S. Tanaka, *J. Phys. Soc. Jpn.* **51**, 219 (1982).
- [17] D. E. Moncton, J. D. Axe, and F. J. DiSalvo, *Phys. Rev. Lett.* **34**, 734 (1975).
- [18] H. Suderow, V. G. Tissen, J. P. Brison, J. L. Martínez, and S. Vieira, *Phys. Rev. Lett.* **95**, 117006 (2005).
- [19] R. H. Friend and D. Jerome, *J. Phys. C: Solid State Phys.* **12**, 1441 (1979).
- [20] I. Kantor, V. Prakapenka, A. Kantor, P. Dera, A. Kurnosov, S. Sinogeikin, N. Dubrovinskaia, and L. Dubrovinsky, *Rev. Sci. Instrum.* **83**, 125102 (2012).
- [21] R. Boehler and K. De Hantsetters, *High Pressure Res.* **24**, 391 (2004).
- [22] A. F. Goncharov, J. M. Zaug, J. C. Crowhurst, and E. Gregoryanz, *J. Appl. Phys.* **97**, 094917 (2005).
- [23] Y. Fei, A. Ricolleau, M. Frank, K. Mibe, G. Shen, and V. Prakapenka, *Proc. Natl. Acad. Sci. U.S.A.* **104**, 9182 (2007).
- [24] See Supplemental Material at <http://link.aps.org/supplemental/10.1103/PhysRevB.102.064105> for supplemental figures and table.
- [25] CrysAlisPro Software system, version 1.171.38.46, Rigaku, 2017.
- [26] O. V. Dolomanov, L. J. Bourhis, R. J. Gildea, J. A. K. Howard, and H. Puschmann, *J. Appl. Crystallogr.* **42**, 339 (2009).
- [27] G. Sheldrick, *Acta Crystallogr., Sect. A* **64**, 112 (2008).
- [28] V. Petricek, M. Dusek, and L. Palatinus, *Z. Kristallogr. Cryst. Mater.* **229**, 345 (2014).
- [29] K. D. Bronsema, J. L. De Boer, and F. Jellinek, *Z. Anorg. Allg. Chem.* **540**, 15 (1986).
- [30] J. Ying, H. Paudyal, C. Heil, X.-J. Chen, V. V. Struzhkin, and E. R. Margine, *Phys. Rev. Lett.* **121**, 027003 (2018).
- [31] L. Su, C.-H. Hsu, H. Lin, and V. M. Pereira, *Phys. Rev. Lett.* **118**, 257601 (2017).
- [32] D. Mou, A. Sapkota, H. H. Kung, V. Krapivin, Y. Wu, A. Kreyssig, X. Zhou, A. I. Goldman, G. Blumberg, R. Flint, and A. Kaminski, *Phys. Rev. Lett.* **116**, 196401 (2016).
- [33] M. D. Johannes and I. I. Mazin, *Phys. Rev. B* **77**, 165135 (2008).
- [34] M. Calandra and F. Mauri, *Phys. Rev. Lett.* **106**, 196406 (2011).
- [35] M. Rösner, S. Haas, and T. O. Wehling, *Phys. Rev. B* **90**, 245105 (2014).
- [36] A. Bera, A. Singh, D. V. S. Muthu, U. V. Waghmare, and A. K. Sood, *J. Phys.: Condens. Matter* **29**, 105403 (2017).
- [37] V. V. Kechin, *Phys. Rev. B* **63**, 045119 (2001).
- [38] D. Jérôme, T. M. Rice, and W. Kohn, *Phys. Rev.* **158**, 462 (1967).
- [39] F. X. Bronold and H. Fehske, *Phys. Rev. B* **74**, 165107 (2006).
- [40] C. Monney, C. Battaglia, H. Cercellier, P. Aebi, and H. Beck, *Phys. Rev. Lett.* **106**, 106404 (2011).